Nonlinear X-wave formation by femtosecond filamentation in Kerr media

A. Couairon,[1] E. Gaižauskas,[2] D. Faccio,[3] A. Dubietis,[2] and P. Di Trapani[3]
[1]*Centre de Physique Théorique, Centre de la recherche sciencifique UMR 7644, École Polytechnique, F-91128, Palaiseau, France*
[2]*Department of Quantum Electronics, Vilnius University, Sauletekio Avenue, Building 3, LT-10222, Vilnius, Lithuania*
[3]*INFM, Department of Physics and Mathematics, University of Insubria, Via Vallegio 11, I-22100 Como, Italy*
(Received 7 July 2005; revised manuscript received 25 October 2005; published 17 January 2006)

We investigate the formation of X waves during filamentation in Kerr media. From the standard model developed for femtosecond filamentation in liquids, solids, and gases, the influence of several physical effects and parameters is numerically studied in the strongly nonlinear regime where group velocity dispersion alone is insufficient to arrest collapse. The collapse is shown to be arrested by multiphoton absorption and plasma defocusing, but not by dispersion. The postcollapse dynamics takes the form of a pulse splitting, which induces large gradients in the near field and seeds the formation of X waves, appearing both in the near and far fields. We discuss the universal features of the X-wave patterns, among which the long arms in the far field that follow the linear dispersive properties of the medium [Conti *et al.*, Phys. Rev. Lett. **90**, 170406 (2003); Kolesik *et al.*, Phys. Rev. Lett. **92**, 253901 (2004)] and are accompanied by a strong modulated axial emission.

DOI: 10.1103/PhysRevE.73.016608 PACS number(s): 42.65.Tg, 42.65.Jx

I. INTRODUCTION

The phenomenon of femtosecond filamentation has now attracted attention for about one decade [1–16]. Despite considerable literature on the subject reporting generation of filaments in various media, at various wavelengths and pulse durations or energies, several different interpretations of this phenomenon still coexist, precisely because of the diversity in the experimental conditions. Initially, femtosecond filamentation was discovered from the propagation in air or gases of subpicosecond laser pulses with power exceeding the critical power for self-focusing $P_{\mathrm{cr}} \equiv 3.77\lambda_0^2/8\pi n_0 n_2$ (3 GW in air) [17]. Here, λ_0 denotes the laser wavelength, n_0 denotes the linear index of the medium, and n_2 its nonlinear coefficient. Instead of a beam collapse and a breakdown of the gas, the pulse was observed to form one or several narrow structures with a hot core (diameter of about 100 μm) able to propagate over extended distances, without apparent diffraction [1]. Femtosecond filamentation was later shown to occur also in transparent solids such as fused silica [18]. This type of media have a nonlinear index coefficient usually 3 orders of magnitude larger than gases, making possible the femtosecond filamentation process with energies in the micro-Joule range. The filaments generated in condensed media exhibit a narrower hot core than in gases, and hence, they are suitable candidates for applications requiring the deposition of laser energy over a limited scale in a bulk medium, such as the production of buried optical elements. Filamentation in solids, is, indeed, intrinsically linked to damage because saturation of self-focusing usually produces intensities and fluences comparable to the known thresholds for damage [6]. From a fundamental point of view, the short Rayleigh length associated to filaments in condensed media allows studies of the phenomenon over reduced scales. To this aim, damage or heating of the material should be avoided by moving the sample continuously so that the successive pulses interact with fresh material. Water, however, constitutes an alternative condensed medium in which femtosecond filamentation was recently demonstrated [10]. The advantage of liquids is that the sample is not damaged by successive laser shots. Both liquids and solids share the property of having a large nonlinear index coefficient and large dispersive coefficients. Until recently, the physics of filamentation in gases and in condensed media was assumed, and actually shown, to be generic and universal [14], i.e., proceeding from an interplay between mainly diffraction, self-focusing due to the optical Kerr effect, and plasma defocusing, while the participation of other physical effects such as chromatic dispersion and multiphoton absorption (MPA), although visible, was considered as only slightly affecting the interplay of the main mechanisms. Among possible reasons, there is certainly the fact that measurements of the filamentation dynamics, as well as models, aim at exhibiting the role of the most visible high intensity part of the wave.

Recent results show, however, that experimental measurements of filamentation in water can be reproduced with good agreement by using a model exhibiting an interplay between different main physical effects [13]. These effects are diffraction, self-focusing, and nonlinear losses (NLL) which correspond to multiphoton absorption that does not necessarily lead to plasma generation, as is the case when the laser pulse leaves the medium in an excited electronic state.

In a model, parameters characterizing each physical effect must usually be introduced but are not always known with a great precision and the conclusion regarding the physical effects that prevail in filamentation obviously depends on the choice of these parameters, in particular when a good agreement with measurements is obtained in a whole parameter range. From recent works, it is now well established that a signature of filamentation in water and in transparent solids is the X-wave generation in normally dispersive media, the role of which in the dynamics of filamentation is still an open question [16,19]. The notion of X waves was originally introduced as a solution to stationary, nondiffractive and nondispersive, linear propagation problems in dispersive extended media [20]. These waves possess a biconical shape

(an **X**) both in the space-time domain (for the near field) and in the wave-number-frequency domain (for the far field). Recently, the existence of nonlinear X-waves has been shown for a nonlinear propagation model (nonlinear Schrödinger equation) including group velocity dispersion [21]; these waves are more generally nondispersive and nondiffractive stationary solutions of a nonlinear propagation problem and have a high intensity core surrounded by extended biconical feet. Kolesik and co-workers [19] have shown that filamentation in water forms X-wave patterns, called dynamic X waves, appearing in the far fields only. The dynamic X waves were shown to result from the competition between group velocity dispersion and Kerr self-focusing while the near fields exhibit successive focusing defocusing cycles following the dynamic spatial replenishment model [4]. The recent measurement of X-like patterns both for the near field and the far field of light filaments in water [22] suggests that nonlinear X waves [21] might be considered as the ultimate state reached by dynamic X waves [19], both types of waves sharing universal features detailed below. This provides a new insight in the physics of filamentation in condensed media and advocates for revisiting the current modeling of this phenomenon. The aim of this paper is to discuss the influence of several physical effects including plasma generation and defocusing, nonlinear losses, group velocity dispersion with its high-order components and pulse self-steepening in the modeling of femtosecond filamentation in transparent Kerr media and in the associated X-wave generation. In so doing, the main criterion used for estimating the importance of each effect is the agreement between computed X-like patterns generated by the propagation of intense laser pulses in Kerr media and the various features of these patterns measured under the same conditions. We, therefore, start by briefly presenting, in Sec. II, the typical features appearing in X-wave measurements during the filamentation process. The outline of the paper is then the following: Sec. III deals with the model used to perform numerical simulations of filamentation in Kerr media. In Sec. IV, it is shown by means of reduced models that several physical effects can arrest the collapse that would occur in a purely Kerr medium and lead to pulse splitting, each subpulse acting as a seed for X-wave generation. Section V focuses on the features of the computed X waves formed by filamentation of infrared laser pulses (800 nm), while Sec. VI deals with filamentation and X-wave generation in water from green laser pulses (527 nm). In both Secs. V and VI, the influence of various physical effects of the features of X waves are discussed.

II. TYPICAL EXPERIMENT ON X-WAVE FORMATION

The input laser pulse is first spatially filtered so as to guarantee a uniform Gaussian-like beam profile that will not break up into multiple filaments. The beam is focused onto the entrance face of a water cell of 5 cm long. The beam waist at this location (referred to as $z=0$ in the following) is $w_0=75$ μm. The pulse undergoes self-focusing and filamentation in the water cell. Angular spectra in the filament are detected by an imaging spectrometer having its entrance slit in the focal plane of a focusing lens, ensuring a single-shot detection of the angular frequency distribution (see Ref. [16] for details).

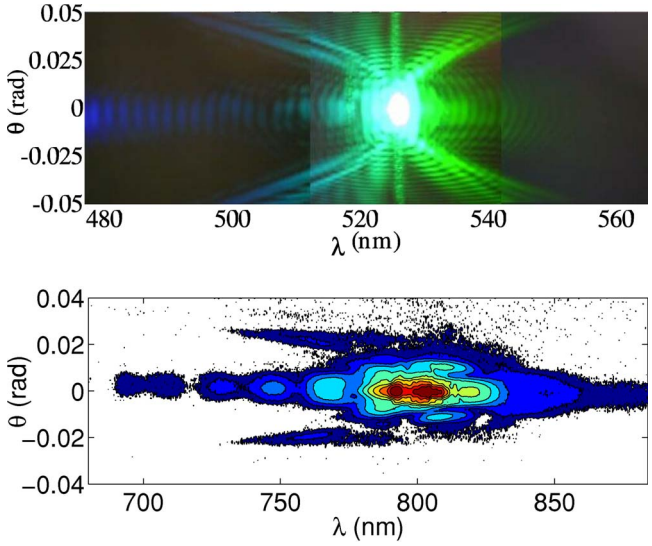

FIG. 1. (Color online) (a) Far field in θ-λ space measured after propagation and filamentation of a green (527 nm) laser pulse over 4 cm in water. (b) same as in (a) for an infrared (800 nm) laser pulse after propagation over 3 cm in water.

Figure 1(a) shows a typical angular spectrum obtained for a $\tau_{FWHM}=200$ fs, green laser pulse ($\lambda_0=527$ nm) with energy $E_{in}=3$ μJ, at the propagation distance of $z=4$ cm. Figure 1(b) shows an angular spectrum obtained at an infrared wavelength ($\lambda_0=800$ nm) for a $\tau_{FWHM}=160$ fs pulse with $E_{in}=3$ μJ.

Specific remarkable features should be noted in both spectra: (i) There is a strong on-axis emission for small transverse wave vectors or angles, extending both into the blue and red regions. (ii) There is an **X** pattern with long arms extending at specific angles, their extension being less pronounced in the redder than in the bluer region for the infrared laser. (iii) The angular spectra are modulated, with fringes exhibiting a paraboliclike dependence on wavelength. These features were found in various media, under different pulse and focusing conditions and can therefore be considered as a signature of filamentation in condensed media.

In the following, we investigate numerically the appearance of these features in the angular spectra by using the standard model presented in Sec. III. In particular, we can use reduce sets of physical effects to determine their contribution in shaping these far-field patterns.

III. PHYSICAL MODEL

The numerical code used in this study relies on the physical model developed for the propagation of an intense pulse in noble gases or air [4,5,9,12], fused silica [6,15,18], and liquids [13,19,22–25].

We model the linearly polarized beam with cylindrical symmetry around the propagation axis z by the envelope $\mathcal{E}$ of the electric field **E**, written as $\mathbf{E}=\mathrm{Re}[\boldsymbol{\mathcal{E}}\exp(ikz-i\omega_0 t)]$,

where $k=n_0\omega_0/c$ and ω_0 are the wave number and frequency of the carrier wave and n_0 denotes the refraction index of water at ω_0. The input pulses are modeled by Gaussians with energy E_{in} and a temporal half width t_p [full width at half maximum (FWHM) duration $\tau_{FWHM}\equiv t_p\sqrt{2\log(2)}$]

$$\mathcal{E}(r,t,0)=\mathcal{E}_0\exp\left(-\frac{r^2}{w_0^2}-\frac{t^2}{t_p^2}\right). \tag{1}$$

The input power is computed from the energy and pulse duration $P_{\text{in}}=E_{\text{in}}/t_p\sqrt{\pi/2}$ and the input intensity is computed from the input power and the transverse waist w_0 of the beam $\mathcal{E}_0^2=2P_{\text{in}}/\pi w_0^2$. The scalar envelope $\mathcal{E}(r,t,z)$ evolves along the propagation axis z according to the nonlinear envelope equation [26], expressed in the frequency domain

$$\hat{U}\frac{\partial\hat{\mathcal{E}}}{\partial z}=i\left[\frac{\nabla_\perp^2}{2k}+\frac{k}{2}\left(\frac{n^2\omega^2}{k^2c^2}-\hat{U}^2\right)\right]\hat{\mathcal{E}}+F_T\{N(\mathcal{E})\}, \tag{2}$$

where $\hat{\mathcal{E}}(r,\omega,z)=F_T\{\mathcal{E}(r,t,z)\}$, $\hat{U}(\omega)\equiv 1+(\omega-\omega_0)/kv_g$, $v_g\equiv\partial\omega/\partial k|_{\omega_0}$ denotes the group velocity and $F_T\{N(\mathcal{E})\}$ denotes the time-Fourier transform of the nonlinear terms. The derivation of Eq. (2) is detailed in the appendix. Equation (2) accounts for diffraction in the transverse plane, space-time focusing (see Refs. [26,27]), group velocity dispersion with high-order terms exactly computed by means of a Sellmeier dispersion relation for the refraction index $n(\omega)$ of water (Eq. (12) in Ref. [28]). The second-order and third-order dispersive terms are obtained by a small $\omega-\omega_0$ expansion of the quantity

$$\hat{U}^{-1}\left(\frac{n^2\omega^2}{k^2c^2}-\hat{U}^2\right)\sim\frac{k''}{k}(\omega-\omega_0)^2+\frac{k'''}{3k}(\omega-\omega_0)^3+\cdots, \tag{3}$$

where the dispersive coefficients are $k''\equiv\partial^2k/\partial\omega^2|_{\omega_0}$ and $k'''\equiv\partial^3k/\partial\omega^3|_{\omega_0}$. When higher-order dispersive terms are neglected as in Sec. V below, Eq. (2) is written in the time domain by using the retarded time $t\equiv t_{\text{lab}}-z/v_g$

$$\frac{\partial\mathcal{E}}{\partial z}=\frac{i}{2k}U^{-1}\nabla_\perp^2\mathcal{E}-i\frac{k''}{2}\frac{\partial^2\mathcal{E}}{\partial t^2}+\frac{k'''}{6}\frac{\partial^3\mathcal{E}}{\partial t^3}+U^{-1}N(\mathcal{E}), \tag{4}$$

where $U\equiv[1+(i/kv_g)(\partial/\partial t)]$.

We consider water, without loss of generality, as a typical Kerr and dispersive medium and two models that include different nonlinearities.

The first model, Eq. (5), includes the optical Kerr effect with possible optical shock terms (self-steepening) and nonlinear losses

$$N(\mathcal{E})=ik_0n_2T^2|\mathcal{E}|^2\mathcal{E}-T\frac{\beta_K}{2}|\mathcal{E}|^{2K-2}\mathcal{E}. \tag{5}$$

Self-focusing related to the Kerr effect occurs for pulses with P_{in} above P_{cr}. No redshift has been observed in the experiments in water and, therefore, no nonlocal term corresponding to delayed Raman-Kerr contribution [29,30] is taken into account. The operator $T\equiv 1+(i/\omega_0)(\partial/\partial t)$ in front of the Kerr term is responsible for the self-steepening of the pulse (the so-called shock terms) [27,31,32]. For the sake of understanding the importance of each effect individually, the nonlinear losses correspond to a multiphoton absorption term that does not induce multiphoton ionization (MPI), but only excitation of the water molecules. In this respect, note that there is no coupling with a plasma density in model (5) even if the dependence of NLL on intensity is the same as for MPI-induced losses.

In the second model, Eq. (6), the nonlinear effects include the optical Kerr effect again with possible shock terms, plasma absorption, plasma defocusing, and multiphoton absorption

$$N(\mathcal{E})=ik_0n_2T^2|\mathcal{E}|^2\mathcal{E}-\frac{\sigma(\omega)}{2}(1+i\omega\tau_c)\rho\mathcal{E}-T\frac{\beta_K}{2}\left(1-\frac{\rho}{\rho_{\text{n}}}\right)\times|\mathcal{E}|^{2K-2}\mathcal{E}. \tag{6}$$

In the following, model (5) will be referred to as the model without plasma and model (6) as the model with plasma defocusing. The model (6) is coupled with the density ρ of the electron plasma generated by multiphoton ionization or avalanche, the evolution of which is governed by Eq. (7)

$$\frac{\partial\rho}{\partial t}=\sigma_K|\mathcal{E}|^{2K}(\rho_{\text{n}}-\rho)+\frac{\sigma}{U_i}\rho|\mathcal{E}|^2. \tag{7}$$

The first term on the right hand side of Eq. (7) describes electron-hole plasma generation via multiphoton processes. The quantity ρ_{n} denotes the density of neutral molecules of water. The potential U_i for water corresponds to a transition from the $1b_1$ molecular orbital to an exciton band [33–35] and $K\equiv\langle(U_i/\hbar\omega_0)+1\rangle$ (where $\langle\cdots\rangle$ denotes the integer part) is the number of photons involved in the multiphoton process. In Eq. (7), the transition rate σ_K reads is linked to the multiphoton absorption cross section: $\beta_K=\sigma_K\times K\hbar\omega_0\rho_{\text{n}}$. For sufficiently dense electron-hole plasmas, the avalanche process may generate an electron-ion plasma. The second term in Eq. (7) accounts for avalanche ionization, which involves the cross section for inverse bremsstrahlung σ. This quantity is the same as in the plasma absorption term and follows the Drude model [36]

$$\sigma(\omega)=\frac{e^2}{n_0\omega_0\epsilon_0m_ec}\frac{\omega\tau_c}{1+\omega\tau_c^2}, \tag{8}$$

where the momentum transfer collision time $\tau_c=3$ fs.

We used in all simulations the physical parameters given in Table I unless different values (for β_K and σ_K) are specified in the text. For the dispersive coefficients, the table indicates values inferred from measurements published in the literature [28]. These values have been used for $\lambda_0=800$ nm (Sec. V) while the full dispersion relation (Eq. (12) in Ref. [28]) was used for $\lambda_0=527$ nm (Sec. VI). For the multiphoton absorption coefficient, no direct measurement is available. Its value may be estimated from the Keldysh formulation [37–39]. The accuracy of the estimation is, however, material dependent. For fused silica, for example, values for the multiphoton absorption cross section found in the literature can differ by 4 orders of magnitude one from each other [6]. The table below gives reference values for water, computed from Keldysh's formulation with the given poten-

TABLE I. Parameters used in the model for the two indicated laser wavelengths. The values for n_2 are from Ref. [35,40,41], possibly at slightly different wavelengths (532 nm). The dispersive coefficients are from Ref. [28]. The parameters below the final double space are independent of wavelength. Note that some of the simulations are performed with different parameters that are specified in the text.

λ_0 (nm)	n_0	k'' (fs^2/cm)	k''' (fs^3/cm)
800	1.334	248	270
527	1.340	560	280

λ_0 (nm)	K	β_K (cm^{2K-3} W^{1-K})
800	5	3.5×10^{-50}
527	3	1.2×10^{-23}

λ_0 (nm)	n_2 (cm^2/W)	σ_K (s^{-1} cm^{2K} W^{-K})	P_{cr} (MW)
800	4.1×10^{-16}	4.3×10^{-55}	1.87
527	2.7×10^{-16}	1.5×10^{-28}	1.22

U_i (eV)	ρ_n (cm^{-3})	τ_c (fs)	m^*/m_e
6.5	6.68×10^{22}	3	0.5

tial U_i, and the exciton reduced mass ratio m^*/m_e. Alternatively, the multiphoton absorption coefficient can be deduced from a transmission measurement, such as that performed recently for green laser pulses (527 nm) in water [25]. We used in our calculations several values for the multiphoton absorption cross section that are specified in the text and differ from the value computed from Keldysh's model, first because our recent measurements have shown that a difference amounting to 2 orders of magnitude is plausible, and second for the purpose of illustrating the influence of this parameter [25].

IV. MECHANISMS ARRESTING THE COLLAPSE

In this section, we consider reduced models involving two competing physical effects in addition to diffraction. It will be shown that three different physical mechanisms lead to the arrest of collapse that would occur in a purely Kerr medium. Beyond collapse, the dynamics takes the form of a pulse splitting into two, possibly asymmetric, subpulses departing from each other. Each subpulse constitutes a seed for the generation of an X wave. Specific features of X-wave patterns depend on the velocity of the departing subpulses, i.e., on the relevant mechanism arresting the collapse. We, therefore, detail here the possible candidate for arresting the collapse.

A. Group velocity dispersion

It is well known that group velocity dispersion (GVD) alone is able to arrest the collapse singularity that would occur in a purely Kerr medium [42–45]. This mechanism, however, is relevant for pulses having a sufficiently low peak power or in sufficiently dispersive Kerr media [46]. For the conditions of our simulations (t_p=130 fs, E_{in}=2.2 μJ, λ_0 =800 nm, $P_{in}/P_{cr}\sim7$, w_0=75 μm), GVD of water (k'' =248 fs^2/cm) is not sufficient to arrest collapse as shown in Fig. 2. Here the NLS (Nonlinear Schrödinger equation with GVD limited to second order was integrated

$$\frac{\partial\mathcal{E}}{\partial z}=\frac{i}{2k}\nabla_\perp^2\mathcal{E}-i\frac{k''}{2}\frac{\partial^2\mathcal{E}}{\partial t^2}+ik_0n_2|\mathcal{E}|^2\mathcal{E}. \tag{9}$$

Figure 2(a) shows the beam width (FWHM of the fluence distribution) and Fig. 2(b) shows the peak intensity as a function of the propagation distance for k''=248 fs^2/cm. The collapse singularity at $z\sim6$ mm cannot be avoided. Figures 2(c) and 2(d) show the same quantities for a highly dispersive medium having k''=20 000 fs^2/cm. In this case, the standard arrest of collapse is obtained. The postcollapse dynamics involves a pulse splitting into two components moving in opposite directions in the frame of the input pulse, at velocities

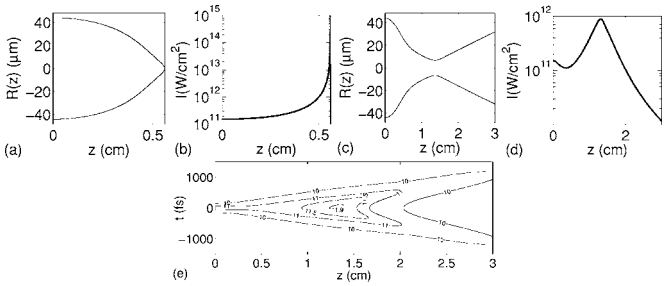

FIG. 2. (a) Beam width and (b) peak intensity as functions of the propagation distance for model (9) and t_p=130 fs, E_{in}=2.2 μJ, λ_0 =800 nm, $P_{in}/P_{cr}\sim7$, w_0=75 μm, and k''=248 fs^2/cm. (c) Beam width and (d) peak intensity obtained with the same parameters but k''=20 000 fs^2/cm. (e) Intensity contours showing pulse splitting in the postcollapse dynamics. The labels 11 and 12 indicate 10^{11} and 10^{12} W/cm^2.

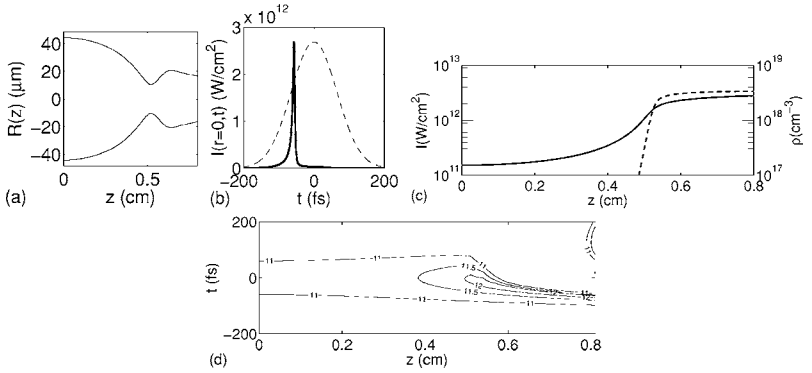

FIG. 3. Arrest of collapse by plasma defocusing computed from model (10): (a) Beam width vs z. (b) On-axis temporal profile for the input pulse (dashed curve) and the pulse at $z=0.72$ cm (continuous curve). (c) Intensity vs z (left axis) and peak electron density vs z (right axis). (d) Contour plot of the on-axis intensity. The parameters are $t_p=130$ fs, $E_{in}=2.2$ μJ, $\lambda_0=800$ nm, $P_{in}/P_{cr}\sim 7$, $w_0=75$ μm, $K=5$, and $\sigma_K=1.2\times 10^{-52}$ s^{-1} cm^{10} W^{-5}.

depending on k'' [see Fig. 2(e)]. In most reasonably dispersive Kerr media, GVD is, therefore, not the relevant mechanism for the arrest of collapse occurring for pulses with relatively large input peak powers.

B. Plasma defocusing

Plasma defocusing constitutes another mechanism arresting the collapse. Here we consider the minimal model

$$\frac{\partial \mathcal{E}}{\partial z}=\frac{i}{2k}\nabla_\perp^2\mathcal{E}+ik_0n_2|\mathcal{E}|^2\mathcal{E}-i\frac{k}{2n_0^2}\frac{\rho}{\rho_c}\mathcal{E}, \tag{10}$$

where the plasma density is generated by multiphoton ionization only [Eq. (7) with $\sigma=0$]. Here, the plasma defocusing term is the same as in Eq. (6) when plasma absorption as well as avalanche ionization are neglected. When $\omega\sim\omega_0$ and $\tau_c\gg\omega_0^{-1}=0.42$ fs at 800 nm, the plasma defocusing term is indeed written as $(\sigma\omega_0\tau_c/2)\rho\mathcal{E}\sim(k\rho/2n_0^2\rho_c)\mathcal{E}$ and involves the critical plasma density above which the plasma becomes opaque $\rho_c\equiv\epsilon_0 m_e\omega_0^2/e^2$.

In contrast with what is generally written in the literature, this model does not lead to the formation of a nonlinear waveguide or a soliton. By integrating Eqs. (10) and (7) with the same Gaussian input pulse as in Sec. IV A, the postcollapse dynamics becomes indeed rapidly singular. Figure 3(a) shows the beam width and Fig. 3(c) the peak intensity and electron density obtained with $\sigma_K=1.2\times 10^{-52}$ s^{-1} cm^{10} W^{-5}(which corresponds to $\beta_K=1\times 10^{-47}$ cm^7 W^{-4}. The collapse is arrested by plasma defocusing, but only the trail of the pulse undergoes the action of the plasma. As shown on Fig. 3(b), the peak intensity is pushed forward as for a superluminal propagation and is shortened continually down to unphysical (subfemtosecond) durations [in the framework of model (10), which does not account for the deviations to the slowly varying envelope approximation]. The contour plot for the on-axis intensity in Fig. 3(d) shows that this model leads to a short peak intensity traveling slightly faster than the light velocity, independently of any dispersive property of the medium.

Plasma defocusing alone is, therefore, able to arrest the collapse but model (10) must be completed by additional physical effects in order to obtain a correct postcollapse dynamics instead of the generation of subfemtosecond pulses.

C. Nonlinear losses

Multiphoton absorption in itself is able to arrest collapse. This was predicted theoretically [47–50]. The minimal model to be considered here reads

$$\frac{\partial \mathcal{E}}{\partial z}=\frac{i}{2k}\nabla_\perp^2\mathcal{E}+ik_0n_2|\mathcal{E}|^2\mathcal{E}-\frac{\beta_K}{2}|\mathcal{E}|^{2K-2}\mathcal{E}. \tag{11}$$

Figures 4(a) and 4(b) show the beam width and the peak intensity as a function of the propagation distance obtained by integrating Eq. (11) from the same Gaussian input pulse as in Sec. IV A, with $K=5$ and $\beta_K=1\times 10^{-47}$ cm^7 W^{-4}. The collapse is clearly arrested around $z\sim 6$ mm and a filamentary propagation follows. Figure 4(c) shows the evolution of the temporal profiles on axis. The pulse is depleted by nonlinear losses. Successive splittings generate a multipeaked structure with large intensity gradients, sufficient to generate a strong on axis emission via self-phase modulation (SPM).

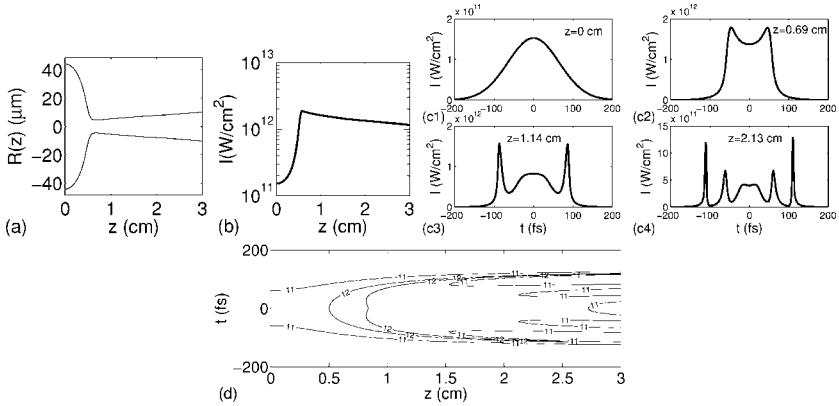

FIG. 4. Arrest of collapse by nonlinear losses computed from model (11): (a) Beam width vs z. (b) Peak intensity vs z. (c) On-axis temporal profiles for the input pulse (dashed curve) and the pulse at $z=0.72$ cm (continuous curve). (d) On-axis intensity distribution. The parameters are $t_p=130$ fs, $E_{in}=2.2$ μJ, $\lambda_0=800$ nm, $P_{in}/P_{cr}\sim 7$, $w_0=75$ μm, $K=5$, and $\beta_5=1\times 10^{-47}$ cm^7 W^{-4}.

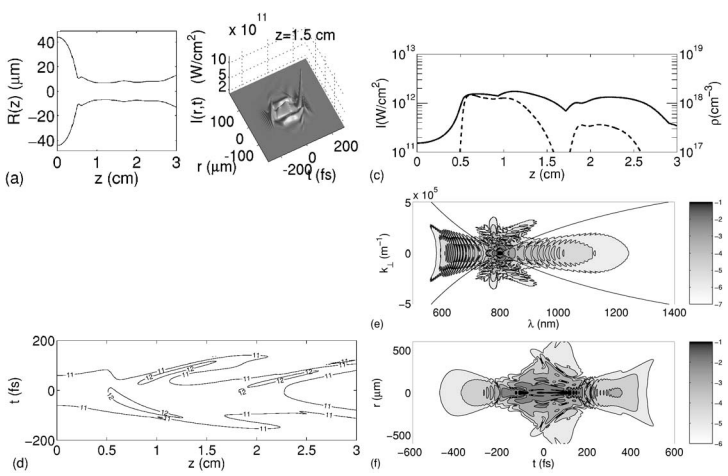

FIG. 5. Arrest of collapse by plasma defocusing and MPA, computed from model (12): (a) Beam width vs z. (b) Intensity distribution at $z=1.5$ cm. (c) Peak intensity (left axis) and electron density (right axis) vs z. (d) On-axis intensity distribution. The parameters are $t_p=130$ fs, $E_{in}=2.2$ μJ, $\lambda_0=800$ nm, $P_{in}/P_{cr}\sim 7$, $w_0=75$ μm, $K=5$, $\sigma_K=1.2\times 10^{-52}$ s^{-1} cm^{10} W^{-5}, and $\beta_5=1\times 10^{-47}$ cm^7 W^{-4}. (e) Far field at $z=3$ cm. (f) Near field at $z=3$ cm. The intensity levels are plotted in logarithmic scale over six or seven decades, the numbers of decades being indicated on the gray-level bar.

The intensity contours in Fig. 4(d) illustrate these recurrent splittings. Note that in this case, the arrest of collapse and the subsequent pulse splitting are obtained for realistic parameters of water.

D. Multiphoton absorption and plasma defocusing

We finally consider the minimal model in which MPA describe the MPI-induced losses, with GVD described up to second order

$$\frac{\partial \mathcal{E}}{\partial z}=\frac{i}{2k}\nabla_\perp^2\mathcal{E}-i\frac{k''}{2}\frac{\partial^2\mathcal{E}}{\partial t^2}+ik_0n_2|\mathcal{E}|^2\mathcal{E}-i\frac{k}{2n_0^2}\frac{\rho}{\rho_c}\mathcal{E}-\frac{\beta_K}{2}|\mathcal{E}|^{2K-2}\mathcal{E}. \tag{12}$$

The beam width [Fig. 5(a)], as well as the peak intensity and electron density [Fig. 5(c)] are computed as functions of the propagation distance by integrating Eqs. (12) and (7) from the same input pulse as previously with the coefficients $n_2=4.1\times 10^{-16}$ cm^2/W, $k''=248$ fs^2/cm, $K=5$ and $\beta_K=1\times 10^{-47}$ cm^7 W^{-4}. Here, both MPA and plasma defocusing are independently able to arrest the collapse, but GVD is not. The arrest of collapse is therefore driven by both MPA and plasma defocusing acting simultaneously. Figure 5(b) shows that the intensity distribution in space and time exhibits an asymmetric two-peaked (in general multipeaked) structure during the postcollapse dynamics. Figure 5(d) shows the on-axis intensity contours with evidence of the asymmetric pulse-splitting dynamics which is due to the fact that the self-focusing of the pulse trail is delayed by the action of the plasma. Each split pulse travels at a specific velocity reflecting the speed of the nonlinear interaction responsible for the splitting. The leading pulse with $t<0$ is faster and the trailing pulse with $t>0$ is slower than the group velocity $v_g(\omega_0)$.

In Ref. [19], a smaller nonlinear index coefficient than in the present work was used and GVD was shown to be the dominant mechanism arresting the collapse and leading to pulse splitting. In contrast, we have shown that with the measured second-order dispersion of water (248 fs^2/cm at 800 nm) and relatively large input peak powers (7 P_{cr}), the mechanisms arresting the collapse are not GVD but MPA and plasma-induced defocusing.

E. Effect of GVD on the postcollapse dynamics and consequences of the pulse splitting on X-wave generation

The highly nonlinear dynamics leading to pulse splitting generates new frequencies via self-phase modulation, which is the origin of a strong on-axis emission. Although minor in the highly nonlinear dynamics near the collapse, the role of GVD is important in the postcollapse dynamics. First, GVD regularizes the large intensity gradients generated by the competition between self-focusing, MPA, and plasma defocusing. No unphysical subfemtosecond structures are generated with model (12). Second, the combined action of GVD and diffraction organizes the less intense part of the wave, i.e., the feets of the near field, as well as the new generated frequencies. Figure 5 shows several generic features for the far field [Fig. 5(e)] and for the near field [Fig. 5(f)] computed by integration of Eq. (12) for a propagation distance of 3 cm. The near field exhibits a clearly visible double-X structure, each X originating from each split pulses emerging after the collapse. Correspondingly, the far field not only exhibits the strong on-axis emission which reflects the new frequencies generated via SPM, but also long arms in the form of a central X. These arms have a slope governed by the dispersive properties of the medium [19,21], i.e., for large departures from the central laser frequency, the angular spectra should be asymptotic to the analytical law $k_\perp=\sqrt{kk''}(\omega-\omega_0)$ shown by the continuous lines in Fig. 5(e). This structure does not appear immediately beyond collapse. The strong on-axis emission generated by SPM appears first, rapidly after collapse, while the central X pattern becomes clearly apparent at larger distances (about twice that needed for col-

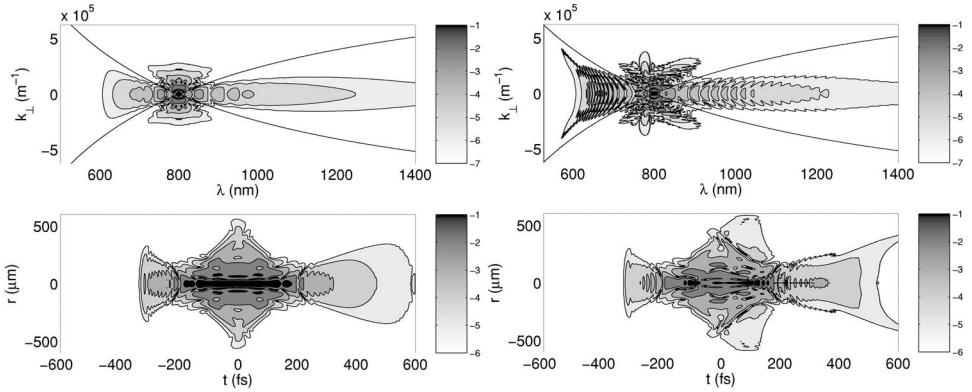

FIG. 6. Far field (top) and near field (bottom) after 3 cm propagation in water computed with dispersive terms up to the third order and no shock terms. First column: no plasma. Second column: same as in first column with plasma generation and plasma defocusing.

lapse in this case). Thus, the wave structure during the postcollapse dynamics is built progressively. The split pulses originating from the arrest of collapse by MPA and plasma defocusing act as a seed for the generation of X waves, the long arms both in the far fields and in the near fields being slowly built by the competition between GVD and diffraction. Finally, the presence of two split pulses in the near field leads to interferences, clearly visible in the far field. Since these split pulses are moving in opposite directions in the reference frame of the input pulse, the far-field X signature generated by each of these split pulses departs from the central X pattern. The deviations actually reflect the details of the nonlinear interaction. As for linear X waves having in general different group and phase velocities than those of a plane pulse of the same frequency in the same material $[v_g(\omega_0)$ and $c/n_0]$ [51], the far-field X signature of each split pulse in the filament possesses two, low and high frequency half-X branches separated by a gap in frequency. The extent of the gap depends on the velocity of each split pulse. These generic features are shown in Fig. 5(e), where the asymptotes of the two half-X branches corresponding to the trailing split pulse intersect the wavelength axis on the blue side around 650 and 750 nm, respectively. On the red side, only the high frequency half-X branch belonging to the leading split pulse is visible with asymptotes intersecting around 850 nm.

These features are similar to the low and high frequency ridges predicted in Ref. [19] except that the splitting dynamics, and hence the frequency gap, was attributed to the effect of GVD, while in our case, GVD determines only the asymptotes of the central X and external half X. A recent study corroborated the presence of two side half-X waves on the blue and red sides of the central X shape in the far field of an infrared pulse filamenting in water. The two halves could be measured with great precision at the expected well-defined wavelengths and were interpreted in terms of a four wave mixing (FWM) process between two highly localized, strong pump waves and two amplifying weak X waves [52].

We end this section by commenting the differences of this FWM model with a three wave mixing (TWM) model involving the optical wave, a material wave accounting for the material excitation and the scattered wave, proposed in Refs. [24,53] to explain the extent of the supercontinuum generation in filamentation.

The visibility of the lowest and highest frequency half-X branches obviously not only depends on the chromatic properties of the material, but also on the frequency gap between the two halves, i.e., on the mechanism and speed of the pulse splitting. In Ref. [53], the phase matching conditions were shown to be compatible with the absence of the red tails of the X far field for a central wavelength of 800 nm, whereas both the red and blue X arms were present for a central wavelength of 400 nm. In Ref. [19], by combining the same three wave mixing model with numerical measurements of the dispersion induced by the material wave, a prediction of the locations of the low and high frequency ridges could be established [19] for a green wavelength of 527 nm. Despite a prediction for the same features in the far fields of filamenting pulses, an essential difference between the FWM and the TWM models is that the dispersion induced by the material wave should be known *a priori* (or obtained from simulations) so as to derive the frequency gap between the half-X waves in the TWM model. In contrast, the FWM model allows an analytical prediction of both the frequency gap between the half-X waves and the group velocities at which the two X waves should travel [52].

V. NUMERICAL SIMULATIONS IN WATER AT 800 NM

In order to investigate numerically the formation of X waves and the influence of several physical effects and parameters on the transformation of the Gaussian input pulses into X waves, we start by comparing models Eq. (5) and Eq. (6), i.e., without and with plasma-induced defocusing, on a typical case for an infrared laser pulse propagating in water, with energy $E_{in}=2.2$ μJ, pulse duration $t_p=130$ fs ($\tau_{FWHM}=153$ fs). The beam waist on the entrance plate of the water cell is $w_0=75$ μm. We will then compare the influence of other physical effects in both models.

A. Influence of plasma defocusing

Figure 6 shows the far-field $\mathcal{E}(k_\perp,\omega,z)$ and the near-field patterns $\mathcal{E}(r,t,z)$ obtained after propagation of the infrared laser pulse with above parameters over a fixed distance $z=3$ cm in the water cell. In these simulations, the cross section for MPA is $\beta_K=1\times10^{-47}$ cm^7/W^4. Group velocity dispersion is described up to the third order. The optical shock terms are not taken into account, which amounts to setting $T=1$ and consistently $U=1$ in the models. Note that both the near and far fields are in logarithmic scale on all figures in this paper, the numbers of decades below the peak intensity being indicated on the gray level bars. The first

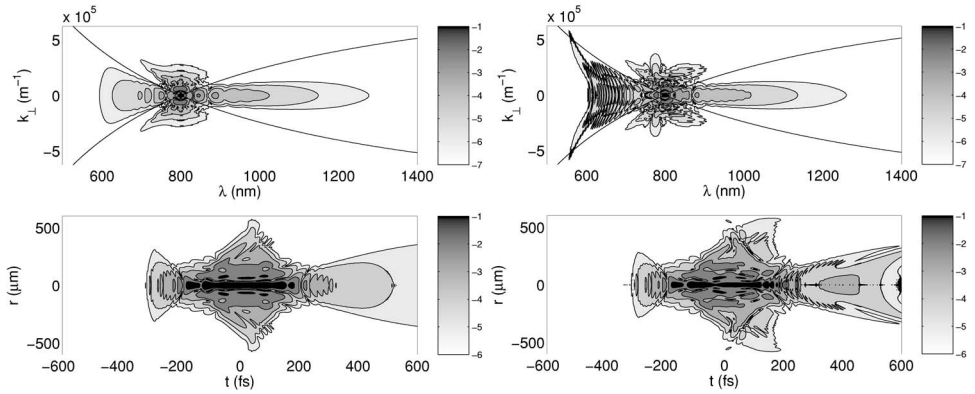

FIG. 7. Far field (top) and near field (bottom) after 3 cm propagation in water as in Fig. 6, but with shock terms in the model and dispersion up to the third order. First column: no plasma, shocks. Second column: plasma, shocks.

column in Fig. 6 corresponds to model Eq. (5) and the second column to model Eq. (6) with plasma-induced defocusing. Both models produce far fields that have an **X** shape centered around 800 nm and a strong on-axis emission. On each far field, the continuous curves indicate the asymptotic direction of the X waves, which follow the dispersive properties of the medium as

$$k_\perp \sim \sqrt{k[k''(\omega-\omega_0)^2 + k'''(\omega-\omega_0)^3/3]}. \tag{13}$$

The near field is constituted by a central core that exhibits two main temporal peaks, each of which having a biconical structure. Interference fringes between these two peaks are visible and produce the modulation that is more visible in the tail, at positive times on the profile computed from model Eq. (6).

The main differences induced by taking into account plasma defocusing are the following. In model (5), the third-order GVD constitutes the single source for the pulse asymmetry in time. In model (6), the pulse asymmetry can be produced either by third-order GVD or by plasma defocusing, which acts on the trailing part of the pulse. It can be readily seen in Fig. 6 that the near field obtained with model (6) is more asymmetric. This asymmetry is in turn visible in the far-field spectra which have an on-axis component with a shorter modulation appearing on both the blue and the red side when plasma-induced defocusing is taken into account. In addition, the extension of the long arms in the far field seem to be promoted by the presence of plasma defocusing in the model (6).

B. Influence of the shock terms

Figure 7 shows the far-field and near-field patterns obtained in the same conditions as in Fig. 6 except for the shock terms that are now taken into account. It can be seen that the main features visible in Fig. 6 are still present, but the modulation in the far field is attenuated for the model including plasma defocusing when shocks are accounted for. Second, for both models, the extent of the on-axis emission with the shock terms is slightly smaller than without shocks. This is consistent with the intuitive notion that the shock term, which in the frequency domain corresponds to the operator $T \equiv 1+(\omega-\omega_0)/\omega_0$, tends to enhance the effective coefficient for SPM for upshifted frequencies, on the blue side of the spectrum, while it reduces this SPM effect on the red side. Therefore, a pulse undergoing the self-steepening effect has a steeper falling edge and will generate more blue than red frequencies via SPM, leading to a blueshifted spectrum with smaller extent in the red part. This slight blueshift in the far fields appear for both models. Finally, this blueshift enhances the asymmetry obtained with the presence of plasma defocusing in model (6), by promoting slightly longer arms on the blue side of the spectra, than their counterparts in Fig. 6.

In the following, all the simulations presented have been done with and without shock terms. Since the differences are never much greater than those observed between Figs. 7 and 6, only the simulations with shock terms are shown on the figures. These small quantitative differences indicate that shock terms, in spite of their importance to describe correctly the extent of the far fields, have much less influence than the uncertainty on some other parameters such as the cross section for multiphoton absorption to cite only one.

Similarly, we have performed all the simulations with the full dispersion relation (Eq. (12) in Ref. [28]) so as to take into account the higher-order dispersive terms. We did not obtain significant changes in the results and, therefore, limit this section to the simulation results at 800 nm with dispersion up to the third order.

C. Influence of the amount of nonlinear losses

Figure 8 shows the far-field and near-field patterns obtained in the same conditions as in Fig. 7, but with a larger value of the cross section for MPA, i.e., $\beta_K = 5 \times 10^{-47}$ cm^7/W^4 instead of $\beta_K = 1 \times 10^{-47}$ cm^7/W^4 in Fig. 7. We used model (5) (first column in Fig. 8) or (6) (second column in Fig. 8).

In model (5), the catastrophic collapse that would have occurred for a pure Kerr model is arrested by NLL; note that group velocity dispersion alone is, in principle, able to arrest collapse but here, the dispersive coefficients for water are sufficiently small that NLL constitutes the prevailing mechanism, as shown in Sec. IV. In model (6), collapse is arrested by both NLL and plasma-induced defocusing. In both cases, the pulse propagates closer to the collapse singularity when the cross section for multiphoton absorption is small. This means that slightly larger intensities are reached near the collapse, which will in turn trigger more efficient nonlinear effects, including self-phase modulation and associated

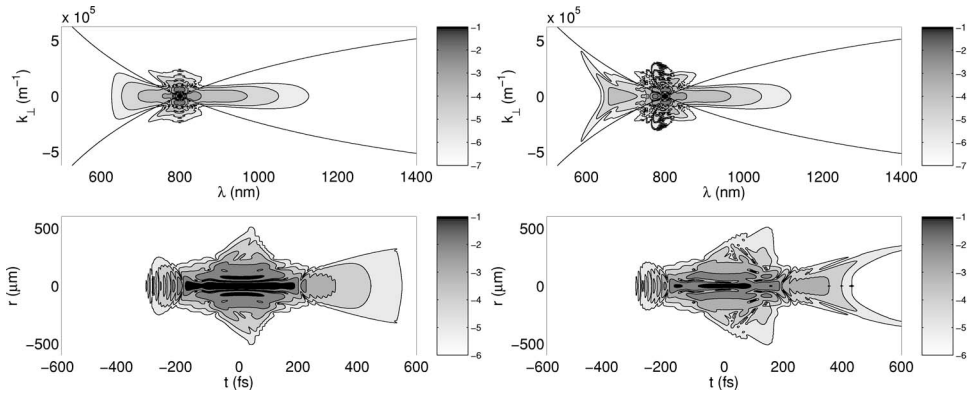

FIG. 8. Same as in Figs. 6 and 7 for $\beta_K=5\times10^{-47}$ cm^7 W^{-4}. First column: no plasma. Second column: plasma generation and plasma defocusing are taken into account.

space-time coupling. This constitutes the seed for the transformation of the pulse into X waves during the postcollapse dynamics. Figure 8 exhibits far fields with smaller arms, smaller on-axis emission, weaker modulation although the general features described above are visible. The near fields show similar structures as above with two temporal peaks surrounding feet having a biconical structure in the *r-t* space. The interference between these peaks is weaker.

D. Influence of the pulse energy

Figure 9 shows computed near fields and far fields after propagation over 3 cm in water of a 3 μJ infrared pulse, in the same conditions as in previous figures, but only for model (6) including plasma-induced defocusing. Pulses with larger energy and the same duration have a larger peak power corresponding here to a jump from 7 to 11 P_{cr}. Self-focusing is, therefore, more efficient, which results in a faster focusing-defocusing dynamics. The near fields exhibit more pronounced temporal pulse splitting than their counterpart at lower energy, resulting also in a fringe pattern with a better contrast. The smallest value for $\beta_K=1\times10^{-47}$ cm^7/W^4 was used in the first column and the largest value in the second column. It can be seen that the extension of the long arms in the far fields is larger on the first column, with the smallest β_K. This is due to the fact that during the self-focusing stage, steeper gradients are generated in the near field when a small β_K is used, because the collapse process is arrested later, whatever the nonlinear mechanism prevailing in the arrest process. (Note that the same quantity β_K is linked to the efficiency of both arrest mechanisms: plasma defocusing and multiphoton absorption.)

VI. NUMERICAL SIMULATIONS IN WATER AT 527 NM

A. Typical calculation at 527 nm

Similar trends are observed at other wavelengths. For instance, Fig. 10 shows the computed far field and near field of a 527 nm, $\tau_{FWHM}=200$ fs laser pulse with 2 μJ energy at a propagation distance of 3 cm. Here, the full dispersion relation of water (Eq. (12) in [28]) and shock terms are taken into account. For both models without (first column) or with (second column) plasma-induced defocusing, the far fields exhibit the modulated on-axis emission as well as the central **X** shape with long arms that follows the dispersive properties of the material. The main difference between the models can be seen in the near fields: With plasma-induced defocusing, the pulse underwent more visible and more asymmetric splitting in time. Each subpulse originating from the splitting can be viewed as a single entity building a nonlinear X wave. According to the interpretations given in [19,52], several X waves, with different group velocities, that interact and produce not only the interference fringes and the long feet in the far field but also half-X feet.In the present numerical simulations, the half-X wave appearing around 450 nm in the far fields has its origin in the four wave mixing process between the two intense split pulses, and two X waves with different group velocities. The second half is visible only with much larger dynamical range (four additional decades).

B. Influence of the multiphoton order *K*

Keldysh's formulation for the calculation of the ionization rates and the multiphoton absorption coefficients relies on

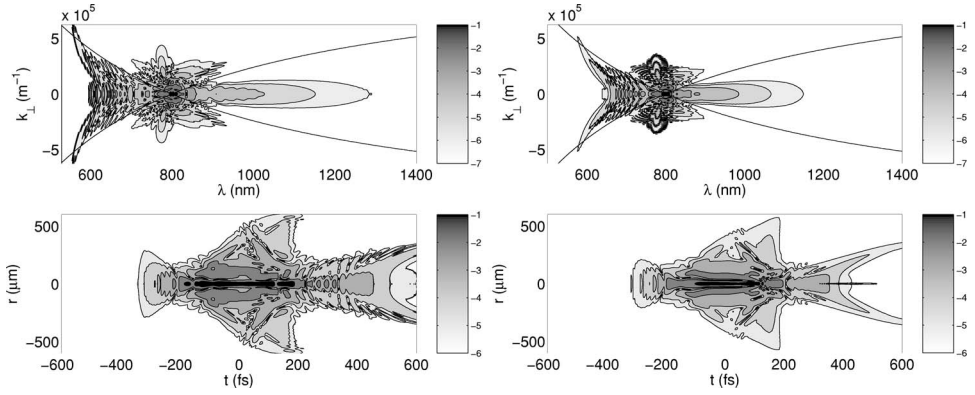

FIG. 9. Same as in second column of Fig. 8 for $E_{in}=3.3$ μJ. Left column $\beta_K=1\times10^{-47}$ cm^7 W^{-4}: right column: $\beta_K=5\times10^{-47}$ cm^7 W^{-4}.

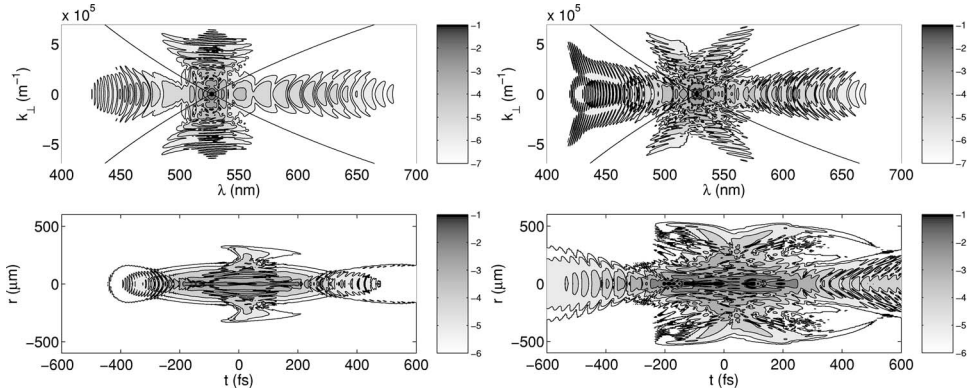

FIG. 10. Far field (top) and near field (bottom) after the propagation of a 2 μJ, 527 nm laser pulse over a distance of 3 cm in water $\beta_3=2\times10^{-24}$ cm^3 W^{-2}. Shocks and high-order dispersive effects are accounted for. First column: no plasma. Second column: same as in first column with plasma generation and plasma defocusing.

several assumptions, among which the specific (non parabolic) band structure of the gap. It is also uncertain whether Keldysh's theory applies to water. With the ionization potential and the effective electron-hole mass specified in Table I, the cross section for multiphoton absorption computed from Keldysh's theory leads to an overestimation of the absorption losses occurring during the propagation of green laser pulses in water. We have shown that our models predict the generation of X waves during filamentation for different values of the cross section for multiphoton absorption, at a specific wavelength. Working with another wavelength for a given band gap allows us to study also the influence of the multiphoton order. Actually, a change in this parameter cannot be completely decoupled from a change in the cross section for MPA because the ionization rate $\sigma_K I^K$ or the multiphoton absorption scaling as $\beta_K I^K$ must keep about the same order of magnitude, since these effects usually act to counterbalance the Kerr effect which is independent of K, σ_K, or β_K. In order to investigate deeper the influence of this parameter, we therefore keep the wavelength of 527 nm and the band gap of 6.5 eV, but allow a variation of K from 3 to 4 and a corresponding variation of β_K. We show in Fig. 11, the near field and the far field computed for the same parameters as in Fig. 10 except for the number of photons and the cross section for multiphoton absorption which were chosen to be $K=4$ and $\beta_4=2\times10^{-36}$ cm^5 W^{-3}. In this case, the general trends are very similar to those already observed with other coefficients with the only difference that the speed of the splitting dynamics is slightly different as well as the extent of the on-axis component of the far fields. These details do not preclude the genericity of the features characterizing the near and far fields. This indicates that for the generation of X waves during filamentation, the specific dependence of the cross section for multiphoton absorption on the intensity is not essential. This dependence, however, determines the strongly nonlinear dynamics occurring immediately beyond the nonlinear focus where filamentation starts, and hence the evolution of the intense core of the near field as well as the speed of the splitting process.

C. Influence of plasma absorption

We have finally studied the influence of plasma absorption on the generation of X waves during filamentation in water. Figure 12 shows the far field and near field computed from model (6) with values for the collision time, τ_c, of 1 fs (left column) and 10 fs (right column), with the same multiphoton absorption as previously ($K=3$ and $\beta_3=2\times10^{-24}$ cm^3 W^{-2}). The main difference observed from the comparison of these figures with those previously obtained concerns the details in the multiple pulse splitting process. Several peaks appear in the near field of Fig. 12(b), as expected from the lower collision time which results in a low plasma absorption while plasma-induced defocusing is more efficient than for $\tau_c=1$ fs. In the far fields, these details in the pulse splitting process leads to corresponding changes in the modulation; the indirect influence of plasma absorption can also be seen in the enhanced blue-side half-X pattern appearing around 430 nm in Fig. 12(b). This brings an additional demonstration that each subpulse appearing in the near field builds an X wave and the resulting far-field pattern can be viewed as an interaction of several X waves, here clearly visible in both the near fields and the far fields, with different positions (central wavelengths) and group velocities.

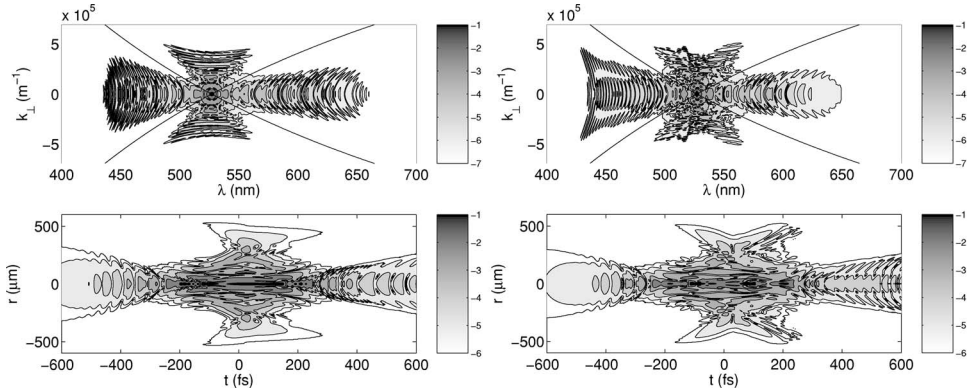

FIG. 11. Same as in Fig. 10 but with the parameters $K=4$ and $\beta_4=2\times10^{-36}$ cm^5 W^{-3}.

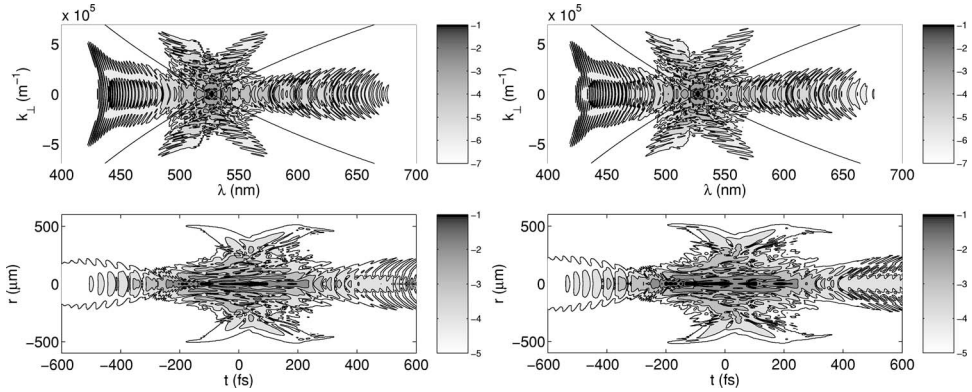

FIG. 12. Same as in second column of Fig. 10 with plasma absorption and avalanche ionization with parameters $\tau_c=1$ fs (first column), and $\tau_c=10$ fs (second column).

VII. CONCLUSION

In conclusion, we have investigated numerically the influence of several physical effects and parameters on the formation of X waves during filamentation in water. The minimal physical effects to be accounted for in order to obtain these X waves numerically are the diffraction, the group velocity dispersion at second order, the optical Kerr effect and any mechanism arresting effectively the collapse (NLL or plasma-induced defocusing). Although several parameters are not known with a great precision, we have shown that in a broad range of parameter values, numerical simulations reproduce the main features of the X-wave patterns measured experimentally under the same conditions for the input pulses. In addition to the long arms in the form of a central X signature in the far field which constitute a nearly universal character [19], strong on-axis emission, modulation of the spectra as well as the high-frequency half-X predicted from a four wave mixing interpretation [52] are obtained numerically. Yet a better knowledge of the physical parameters entering in the model would certainly lead to a better quantitative agreement. The far fields and near fields presented in this paper are all plotted in logarithmic scale, which visually enhances the importance of the long arms and of the red and blue half-X components. This makes some features apparent in the simulation results but not necessarily observed in measured far fields which have a smaller dynamic range. For example, the red tails of the central X pattern at 800 nm are missing on Fig. 1(b). In this respect, note that it was not sufficient to take account of higher-order dispersive coefficients or even the full dispersion relation [28] so as to reproduce the measurements. However, an artificially increased third-order dispersive coefficient in the model allows attenuation of the numerically computed red tails. The absence of these red tails in experiments might also be due to an imperfect input Gaussian pulse or to a possible frequency dependence of the multiphoton absorption. Our simulations, therefore, show that the importance of the exact chromatic dispersion to limit the spectral extent of the supercontinuum generation, first pointed out in Ref. [24], can be shadowed by that of the strong nonlinear effects acting as a seed for the generation of the X waves. The spectral extent of the supercontinuum is linked to the efficiency of the seed, which again advocates for a better knowledge of the effective ionization rates and more generally the physical parameters in our model. A recent study even suggested that the chromatic properties of the medium are modified by plasma-induced defocusing [54]; the effect indeed modifies the refraction index as $\delta n=-\omega_p^2/\omega^2$, which clearly indicates a stronger influence on the red part of the spectrum.

A common trend with the measurements is the fact that the structure of the numerically computed X waves is more or less stable in the sense that these features appear in the far field beyond the arrest of the collapse, whatever the mechanism arresting the collapse. Then they evolve only slowly while the near-field pattern can exhibit recurrent nucleation and extinction of temporal peaks or subpeaks, the recurrence being accelerated at large energies of the input pulses or by lowering the various coefficients linked to the absorption of energy.

The recurrent nucleation of substructures in the near field is in agreement with the model of the laser energy reservoir [55] according to which the hot core of the wave contains and dissipates slowly a fraction of the total energy via NLL, mainly during the filamentation stage producing intense peaks, while the cold and extended part of the wave continually refills the hot core owing to self-focusing. This competition between strong nonlinear processes is accompanied by important organization of the visible low-intensity parts of the wave in which linear processes such as diffraction and dispersion prevail. This organization of the wave structure during filamentation slowly transforms the Gaussian pulse initially localized in the physical as well as the spectral space, into an extended, weakly localized wave. Despite the seemingly stationary state observed and computed in the far fields, these processes rule out the possibility that a solitary wave, which is intrinsically localized in space and time, governs the evolution of the laser field during filamentation.

APPENDIX: DERIVATION OF THE PROPAGATION EQUATION

Equation (2) is obtained from the wave equation in a dispersive medium including the nonlinear response of the medium (polarization and current)

$$(\partial_z^2+\nabla_\perp^2)\mathbf{E}(\mathbf{r},t)-\frac{1}{c^2}\partial_t^2\int_{-\infty}^{t}dt' n^2(t-t')\mathbf{E}(\mathbf{r},t')$$
$$=\mu_0\partial_t^2\mathbf{P}_{nl}+\mu_0\partial_t\mathbf{J}. \quad \text{(A1)}$$

The laser field is written as the superposition of the carrier wave and envelope

$$E(\mathbf{r},t) = \mathcal{E}(\mathbf{r},t)\exp[i(\beta_0 z - \omega_0 t + \Psi_0)] + \text{c . c . ,}$$

where we follow the notation of Ref. [26]: $\kappa(\omega) \equiv n(\omega)\omega/c$, $\beta_m + i\alpha_m = (\partial^m \kappa)/(\partial \omega^m)|_{\omega_0}$. The propagation equation of the envelope then reads

$$(-\beta_0^2 + 2i\beta_0\partial_z + \partial_z^2 + \nabla_\perp^2)\mathcal{E} + (\beta_0 + i\beta_1\partial_t + L)^2\mathcal{E} = -\frac{\omega_0^2}{\epsilon_0 c^2}T^2\mathcal{P}_{nl} - i\frac{\omega_0}{\epsilon_0 c^2}T\mathcal{J}, \tag{A2}$$

where

$$L = i\alpha_0 - \alpha_1\partial_t + \sum_{m=2}^{+\infty}\frac{\beta_m + i\alpha_m}{m!}(i\partial_t)^m$$

and

$$T \equiv 1 + i\omega_0^{-1}\partial_t, \tag{A3}$$

and

$$\mathcal{P}_{nl} = 2\epsilon_0 n_0 n_2 |\mathcal{E}^2|\mathcal{E}, \tag{A4}$$

$$T\mathcal{J} = n_0\epsilon_0 c[\sigma(\omega)(1 + i\omega\tau_c)\rho\mathcal{E} + T\beta_K|\mathcal{E}|^{2K-2}\mathcal{E}]. \tag{A5}$$

In the reference frame of the laser pulse ($\tau = t - \beta_1 z, \xi = z$), the left hand side of the propagation equation reads, after the transformation $\partial_z = \partial_\xi - \beta_1\partial_\tau$, $\partial_t = \partial_\tau$,

$$\left(1 + i\frac{\beta_1}{\beta_0}\partial_\tau\right)(\partial_\xi - iL)\mathcal{E} + \frac{1}{2i\beta_0}\nabla_\perp^2\mathcal{E} + \frac{1}{2i\beta_0}(\partial_\xi^2 + L^2)\mathcal{E}.$$

The second derivative $\partial_{\xi^2}^2$ can be neglected in the paraxial approximation. In the Fourier space corresponding to the delayed time τ, it is convenient to introduce $\hat{L}(\omega)$, the Fourier transform of L which includes all high-order dispersive terms, and the operator

$$\hat{U}(\omega) = 1 + \frac{\beta_1}{\beta_0}(\omega - \omega_0) = \frac{\beta(\omega) - \hat{L}(\omega)}{\beta_0}.$$

The propagation equation (2) is then recovered

$$\hat{U}(\omega)\partial_\xi\hat{\mathcal{E}} = \frac{i}{2\beta_0}\nabla_\perp^2\hat{\mathcal{E}} + i\frac{\beta_0}{2}\left[\frac{\beta^2(\omega)}{\beta_0^2} - \hat{U}^2\right]\hat{\mathcal{E}} + F_T[N(\mathcal{E})],$$

where $N(\mathcal{E}) \equiv i(\beta_0/2n_0^2\epsilon_0)T^2\mathcal{P}_{nl} - (1/2n_0\epsilon_0 c)T\mathcal{J}$.

The operator which describes space-time focusing (U^{-1} in front of diffraction), therefore, involves the group velocity, while self-steepening is accounted for by the operator $U^{-1}T^2$ in front of the Kerr term. In a condensed media, this makes a difference with the standard approximation $U \sim T$ [26].

[1] A. Braun, G. Korn, X. Liu, D. Du, J. Squier, and G. Mourou, Opt. Lett. **20**, 73 (1995).
[2] E. T. J. Nibbering, P. F. Curley, G. Grillon, B. S. Prade, M. A. Franco, F. Salin, and A. Mysyrowicz, Opt. Lett. **21**, 62 (1996).
[3] A. Brodeur, C. Y. Chien, F. A. Ilkov, S. L. Chin, O. G. Kosareva, and V. P. Kandidov, Opt. Lett. **22**, 304 (1997).
[4] M. Mlejnek, E. M. Wright, and J. V. Moloney, Opt. Lett. **23**, 382 (1998).
[5] A. Couairon, S. Tzortzakis, L. Bergé, M. Franco, B. Prade, and A. Mysyrowicz, J. Opt. Soc. Am. B **19**, 1117 (2002).
[6] L. Sudrie, A. Couairon, M. Franco, B. Lamouroux, B. Prade, S. Tzortzakis, and A. Mysyrowicz, Phys. Rev. Lett. **89**, 186601 (2002).
[7] P. Sprangle, J. R. Peñano, and B. Hafizi, Phys. Rev. E **66**, 046418 (2002).
[8] D. Mikalauskas, A. Dubietis, and R. Danielus, Appl. Phys. B: Lasers Opt. **75**, 899 (2002).
[9] A. Couairon, G. Méchain, S. Tzortzakis, M. Franco, B. Lamouroux, B. Prade, and A. Mysyrowicz, Opt. Commun. **225**, 177 (2003).
[10] A. Dubietis, G. Tamošauskas, I. Diomin, and A. Varanavičius, Opt. Lett. **28**, 1269 (2003).
[11] M. Kolesik and J. V. Moloney, Opt. Lett. **29**, 590 (2004).
[12] G. Méchain, A. Couairon, M. Franco, B. Prade, and A. Mysyrowicz, Phys. Rev. Lett. **93**, 035003 (2004).
[13] A. Dubietis, E. Gaižauskas, G. Tamošauskas, and P. Di Trapani, Phys. Rev. Lett. **92**, 253903 (2004).
[14] H. Schroeder and S. L. Chin, Opt. Commun. **234**, 399 (2004).
[15] A. Couairon, L. Sudrie, M. Franco, B. Prade, and A. Mysyrowicz, Phys. Rev. B **71**, 125435 (2005).
[16] D. Faccio, P. Di Trapani, S. Minardi, A. Bramati, F. Bragheri, C. Liberale, V. Degiorgio, A. Dubietis, and A. Matijosius, J. Opt. Soc. Am. B **22**, 862 (2005).
[17] J. H. Marburger, Prog. Quantum Electron. **4**, 35 (1975).
[18] S. Tzortzakis, L. Sudrie, M. Franco, B. Prade, A. Mysyrowicz, A. Couairon, and L. Bergé, Phys. Rev. Lett. **87**, 213902 (2001).
[19] M. Kolesik, E. M. Wright, and J. V. Moloney, Phys. Rev. Lett. **92**, 253901 (2004).
[20] P. Saari and K. Reivelt, Phys. Rev. Lett. **79**, 4135 (1997).
[21] C. Conti, S. Trillo, P. Di Trapani, G. Valiulis, A. Piskarskas, O. Jedrkiewicz, and J. Trull, Phys. Rev. Lett. **90**, 170406 (2003).
[22] D. Faccio, A. Matijosius, A. Dubietis, R. Piskarskas, A. Varanavičius, E. Gaižauskas, A. Piskarskas, A. Couairon, and P. Di Trapani, Phys. Rev. E **72**, 037601 (2005).
[23] Q. Feng, J. V. Moloney, A. C. Newell, E. M. Wright, K. Cook, P. K. Kennedy, D. X. Hammer, B. A. Rockwell, and C. R. Thompson, IEEE J. Quantum Electron. **33**, 127 (1997).
[24] M. Kolesik, J. V. Moloney, G. Katona, and E. M. Wright, Appl. Phys. B: Lasers Opt. **77**, 185 (2003).
[25] A. Dubietis, A. Couairon, E. Kučinskas, G. Tamošauskas, E. Gaižauskas, D. Faccio, and P. Di Trapani (unpublished).
[26] T. Brabec and F. Krausz, Phys. Rev. Lett. **78**, 3282 (1997).
[27] A. L. Gaeta, Phys. Rev. Lett. **84**, 3582 (2000).
[28] A. G. Van Engen, S. A. Diddams, and T. S. Clement, Appl. Opt. **37**, 5679 (1998).

[29] R. H. Stolen, J. P. Gordon, W. J. Tomlison, and H. A. Haus, J. Opt. Soc. Am. B **6**, 1159 (1989).
[30] G. K. L. Wong and Y. R. Shen, Phys. Rev. A **10**, 1277 (1974).
[31] A. A. Zozulya, S. A. Diddams, and T. S. Clement, Phys. Rev. A **58**, 3303 (1998).
[32] A. A. Zozulya, S. A. Diddams, A. G. Van Engen, and T. S. Clement, Phys. Rev. Lett. **82**, 1430 (1999).
[33] A. Migus, Y. Gauduel, J. L. Martin, and A. Antonetti, Phys. Rev. Lett. **58**, 1559 (1987).
[34] F. Williams, S. P. Varna, and S. Hillenius, J. Chem. Phys. **64**, 1549 (1976).
[35] P. K. Kennedy, IEEE J. Quantum Electron. **31**, 2241 (1995).
[36] E. Yablonovitch, Phys. Rev. A **10**, 1888 (1974).
[37] L. V. Keldysh, Zh. Eksp. Teor. Fiz. **47**, 1945 (1964).
[38] A. M. Perelomov, V. S. Popov, and M. V. Terent'ev, Zh. Eksp. Teor. Fiz. **50**, 1393 (1966).
[39] K. Mishima, M. Hayashi, J. Yi, S. H. Lin, H. L. Selzle, and E. W. Schlag, Phys. Rev. A **66**, 033401 (2002).
[40] D. N. Nikogosyan, *Properties of Optical and Laser-Related Materials* (Wiley, Chichester, 1997).
[41] W. L. Smith, P. Liu, and N. Bloembergen, Phys. Rev. A **15**, 2396 (1977).
[42] P. Chernev and V. Petrov, Opt. Lett. **17**, 172 (1992).
[43] J. E. Rothenberg, Opt. Lett. **17**, 583 (1992).
[44] N. A. Zharova, A. G. Litvak, T. A. Petrova, A. M. Sergeev, and A. D. Yunakovskii, JETP Lett. **44**, 13 (1986).
[45] N. A. Zharova, A. G. Litvak, and V. A. Mironov, JETP Lett. **75**, 539 (2002).
[46] G. G. Luther, J. V. Moloney, A. C. Newell, and E. M. Wright, Opt. Lett. **19**, 862 (1994).
[47] B. J. LeMesurier, Physica D **138**, 334 (2000).
[48] S. N. Vlasov, L. V. Piskunova, and V. I. Talanov, Zh. Eksp. Teor. Fiz. **95**, 1945 (1989).
[49] N. E. Kosmatov, V. F. Shvets, and V. E. Zakharov, Physica D **52**, 16 (1991).
[50] S. Dyachenko, A. C. Newell, A. Pushkarev, and V. E. Zakharov, Physica D **57**, 96 (1992).
[51] M. A. Porras and P. Di Trapani, Phys. Rev. E **69**, 066606 (2004).
[52] D. Faccio, M. Porras, A. Dubietis, F. Bragheri, A. Couairon, and P. Di Trapani, physics/0510212v1 (unpublished).
[53] M. Kolesik, G. Katona, J. V. Moloney, and E. M. Wright, Phys. Rev. Lett. **91**, 043905 (2003).
[54] I. G. Koprinkov, Appl. Phys. B: Lasers Opt. **79**, 359 (2004).
[55] M. Mlejnek, M. Kolesik, J. V. Moloney, and E. M. Wright, Phys. Rev. Lett. **83**, 2938 (1999).